Ultrasensitive *in Vivo* Detection of Primary Gastric Tumor and Lymphatic Metastasis Using Upconversion Nanoparticles

Ruirui Qiao,[†,⊥] Changhao Liu,[‡,⊥] Muhan Liu,[§] Hao Hu,[‡] Chunyan Liu,[†] Yi Hou,[†] Kaichun Wu,[*,‡] Yenan Lin,[§] Jimin Liang,[§] and Mingyuan Gao[*,†]

[†]Institute of Chemistry, Chinese Academy of Sciences, Bei Yi Jie 2, Zhong Guan Cun, Beijing 100190, China, [‡]State Key Laboratory of Cancer Biology, Xijing Hospital of Digestive Diseases, Fourth Military Medical University, Xi'an 710032, China, and [§]Life Sciences Research Center, School of Life Sciences and Technology, Xidian University, Xi'an 710071, China. [⊥]These authors contributed equally to this work.

ABSTRACT Lymphatic metastasis is an important prognostic factor regarding long-term survival rate of gastric cancer (GC) patients. Pretreatment knowledge of lymph node status is extremely helpful for planning treatment and prognosis. However, to date, no imaging method has been demonstrated to be effective for detecting lymphatic metastasis in GC. Molecular imaging probes based on upconversion nanoparticles with unique optical and magnetic properties have provided great hope for early tumor detection. Herein we report highly sensitive detection of lymphatic spread using core@shell structured $NaGdF_4$:Yb, Er@$NaGdF_4$ upconversion nanoparticles coated with polyethylene glycol (PEG). A GC-specific probe was constructed through "click" reaction between the maleimide moiety of PEG ligand and the thiol group from partly reduced antigastric cancer antibody MGb_2. The primary tumor and adjacent lymphatic metastasis site were clearly differentiated by upconversion luminescence imaging after the GC-specific probe was delivered through tail vein injection into tumor-bearing mice. Moreover, lymphatic metastases smaller than 1 mm were successfully detected, owing to the ultralow background under 980 nm excitation. It has been demonstrated that both primary and lymphatic metastatic sites in an orthotopic mouse model of human gastric cancer can be optically detected by using GC-specific upconversion luminescence nanoprobes. The current studies may therefore provide a highly effective approach for GC diagnosis.

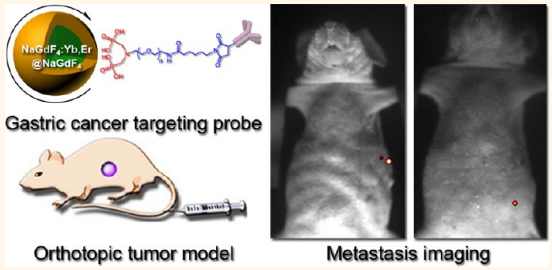

KEYWORDS: ultrasensitive detection · gastric cancer · lymphatic metastasis · upconversion nanoparticles · molecular imaging

Gastric cancer (GC) is the fourth most common malignancy and the second leading cause of cancer mortality worldwide.[1] Early gastric cancer (EGC) is often treated by endoscopical or surgical resection. Due to the high risk of lymph node (LN) metastasis, gastrectomy and lymphadenectomy are normally combined in the treatment of every patient with poorly differentiated EGC. However, the average rate of LN metastasis is no more than 10%.[2] In this context, pretreatment diagnosis of the LN metastasis status would be extremely helpful to avoid patient overtreatment leading to the high morbidity and mortality of the lymphadenectomy. However, it remains a great challenge to detect the LN metastases of GC by using conventional methods.[3]

Molecular imaging provides a great opportunity for early tumor detection and staging upon acquisition of molecular and physiological information.[4,5] Among the ever-increasing modalities, optical imaging based on luminescent or fluorescent probes is widely explored due to the facile and hypersensitive detection of optical signals. However, the detection of conventional fluorescence probes suffers from limited depth of tissue penetration for both excitation and emission lights in the visible range in addition to the high background signal caused by autofluorescence from nontumor tissues. Moreover, the ingested foods may also give rise to strong background signal especially for gastric tumor imaging.[6] Therefore, the conventional optical imaging methods require

* Address correspondence to gaomy@iccas.ac.cn, kaicwu@fmmu.edu.cn.

Received for review December 29, 2014 and accepted January 20, 2015.

Published online January 20, 2015
10.1021/nn507433p

improvement especially for detecting early gastric tumors and metastases.

Recently, upconversion nanoparticles (UCNPs) have shown advantageous optical properties which enable the conversion of low-energy sources in the near-infrared (NIR) region to higher energy light through sequential absorption of multiple photons.[7−10] The unique anti-Stokes mechanism of the upconversion luminescence probes offers greater penetration of tissue by the NIR excitation and eliminates the interference of endogenous fluorescence, giving rise to an enhanced signal-to-noise ratio (SNR). Moreover, with the incorporation of gadolinium in the nanoparticle matrix, dual-modality imaging probes can be constructed with integrated magnetic and upconversion properties.[11−14] The culmination of these physical attributes provides unique opportunities in developing molecular probes for bioimaging, including the analysis of the tumor,[15−18] blood pool,[19] and lymph nodes.[20] Although the toxicity of rare-earth metal ions remains a concern for their *in vivo* applications, previous studies have shown that $NaGdF_4$ nanoparticles do not offer higher level of Gd^{3+} ions in comparison with the clinical contrast agent Gd-DTPA in aqueous solution. Given the fact that Na^+ is highly abundant in human beings, the re-establishment of $NaGdF_4$ decomposition equilibrium will further push the disassociated Gd^{3+} ions down to a much lower level.[12,13] In addition, no significant toxicity of rare-earth nanoparticles to mice has been observed by long-term toxicity experiments based on weight fluctuation and histological and biochemical analyses reported by Li and co-workers.[21]

Apart from imaging modalities, tumor models that can better represent vasculature, pathophysiological processes, and tumor microenvironment are essentially required.[22,23] Owing to the advances in the biocompatible and biofunctionalizable modifications of rare-earth particles, $NaGdF_4$:Yb,Er nanoparticles were successfully used for optical detection of tiny subcutaneous tumors less than 2 mm in diameter *via* active targeting.[8,13] In comparison with subcutaneous tumor models, orthotopic models are highly preferable by showing higher metastatic rates and a more human-analogous microenvironment.[23] Nevertheless, due to the complexity of the model construction and the poor performance of the available nanoprobes, very limited success has been achieved. In a recent study, a GC-specific fluorescence-labeled peptide probe was reported for imaging an orthotopically transplanted gastric tumor.[24] However, the signal was heavily interfered with by the autofluorescence of the surrounding tissue. Therefore, developing advanced optical probes suitable for orthotopic tumor detection remains challenging. We report herein our recent results on molecular imaging of a gastric tumor in an orthotopic tumor model with the use of rare-earth nanoparticles. In brief, core@shell structured $NaGdF_4$:Yb,Er@$NaGdF_4$ nanoparticles were synthesized to further enhance the luminescence intensity of the $NaGdF_4$:Yb,Er core. Following PEGylation, an antigastric tumor antibody MGb_2 was covalently attached to the particle surface to achieve GC targeting specificity. With an orthotopic model, we show that this probe has great potential for GC and metastasis imaging, providing objective diagnosis of lesions in primary and lymphatic metastatic sites with high sensitivity and specificity.

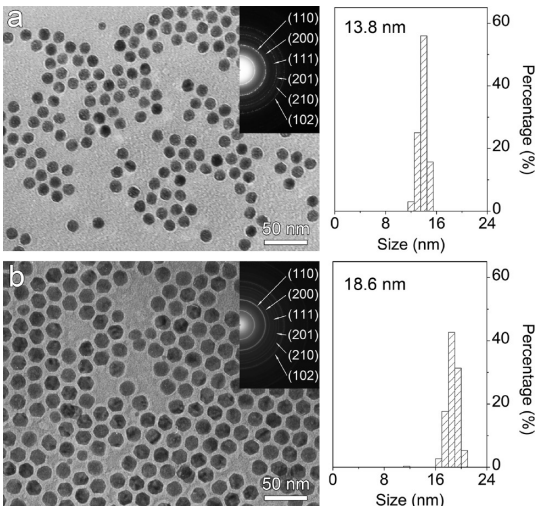

Figure 1. TEM images and size histograms of $NaGdF_4$:Yb,Er core nanoparticles (a) and $NaGdF_4$:Yb,Er@$NaGdF_4$ core@shell nanoparticles (b).

RESULTS

Preparation of Core@Shell $NaGdF_4$:Yb,Er@$NaGdF_4$ Nanoparticles. Doping a Gd^{3+}-containing host matrix with light-emitting rare-earth ions has been demonstrated to be a feasible approach for achieving upconversion luminescent/magnetic particles for both optical and magnetic resonance imaging (MRI) of tumors.[13,18] Toward this demand, core@shell structured $NaGdF_4$:Yb,Er@$NaGdF_4$ particles were prepared by growing a $NaGdF_4$ shell on $NaGdF_4$:Yb,Er core particles prepared according to a previous report.[13] However, such improvements in the photoluminescence (PL) intensity, as yet, have not been demonstrated for increasing the sensitivity of tumor detection and is especially necessary for deep-seated sites.

Figure 1 shows transmission electron microscopy (TEM) images of both core and core@shell particles. The average size of the $NaGdF_4$:Yb,Er core is 13.8 $\pm$ 0.7 nm and effectively increased to 18.6 $\pm$ 0.9 nm after the shell growth. The uniformity of size and shape remain almost unchanged after shell growth. In addition, selected area electron diffraction analysis reveals that both core and core@shell nanoparticles are hexagonal nanocrystals, which is favorable for achieving highly luminescent rare-earth particles.

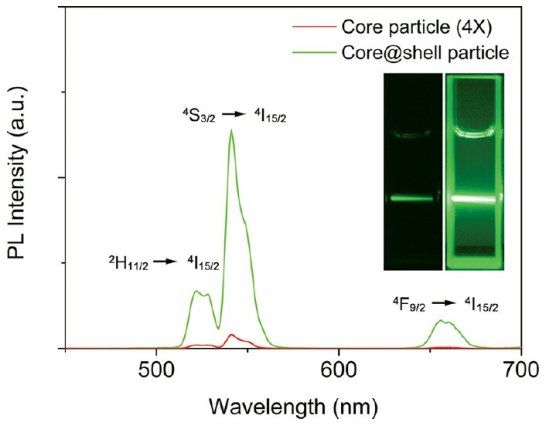

Figure 2. Normalized upconversion luminescence spectra of core particles and core@shell particles in cyclohexane under 980 nm excitation. The insets are full-color photographs of the cyclohexane solutions of the core particles (left) and the core@shell particles (right) taken in the dark under excitation of a 980 nm laser beam.

Optical Properties of the Core@Shell Nanoparticles. Core@shell structures have been demonstrated to be effective for improving luminescence intensity of UCNPs by enhancing the passivation of light-emitting dopants that occurs at the nanoparticle surface.[14,25−29] To verify the effect of the shell coating, emission spectra of both the core nanoparticles and the core@shell structures were characterized under 980 nm laser excitation. Typical upconversion emission peaks located at 521, 541, and 655 nm were observed in the PL spectra of both the core and core@shell nanoparticles. These can be attributed to the energy transfer from $^2H_{11/2}$ and $^4S_{3/2}$ states to the $^4I_{15/2}$ state, generating green emission, and from $^4F_{9/2}$ state to $^4I_{15/2}$ state, generating red emission of Er^{3+}. As displayed in Figure 2, the PL intensity of the core@shell nanoparticles, normalized according to Er^{3+} concentration, is increased by a factor of 70 compared with that for the core nanoparticles, giving rise to very bright green emission as illustrated by the full-color photographs of the nanoparticles in cyclohexane. Such enhanced emission intensity greatly benefits the *in vivo* detection sensitivity.

PEGylation of the UCNPs. Since the as-prepared UCNPs were stabilized by oleate ligands, they were hydrophobic. To overcome the hydrophobicity for the following imaging application, replacement of oleate ligands with an asymmetric polyethylene glycol (PEG) bearing a maleimide group at one end and a diphosphate group at the other (mal-PEG-dp) was carried out according to our previous protocol[12] and provided colloidal stability to the particles in both water and phosphate buffered saline (PBS). Optical studies revealed that the PL intensity of the nanoparticles dropped significantly after being transferred into water, likely due to the high-energy vibration effect of water;[30] however, it remained 57 times higher than that of the PEGylated core nanoparticles, as shown in Figure S1 in Supporting Information. Although the PL intensity loss remains, the overall high PL intensity of the PEGylated core@shell particles is greatly in favor of imaging tissues deeper than otherwise possible.

The surface-associated Gd^{3+} ions additionally endow the nanoparticles with contrast-enhancing effect for MRI. The MRI contrast enhancement effect of both the core and core@shell nanoparticles was characterized on a 3 T MRI instrument. By linear regression fitting of the R_1 values at different Gd^{3+} concentrations, as shown in Figure 3a, the molar relaxivities, r_1, of the PEGylated core and core@shell nanoparticles were determined to be 3.36 and 2.55 mM^{-1} s^{-1}, respectively. The slight decrease of the r_1 value for the core@shell particles can be attributed to the reduced relative surface coverage of Gd^{3+}.[12,31]

Construction of a GC-Specific Probe. For active targeting of a gastric tumor, a highly specific antigastric cancer immunoglobulin G (IgG_1) monoclonal antibody MGb_2[32] was adopted. MGb_2 is a mouse monoclonal antibody developed by immunizing BALB/c mice with the KATOIII gastric cancer cell line. Its antigen identified as TRAK1 (trafficking protein, kinesin-binding 1) is expressed in 81.48% of gastric carcinomas and 100% of signet-ring cell carcinomas, which indicates that MGb_2 is a promising diagnostic targeting molecule for GC.[33] For the construction of a GC-specific probe, MGb_2 was covalently conjugated to the PEGylated UCNPs *via* a "click" reaction between the maleimide group on the particle surface and the thiol group on partly reduced MGb_2. Hydrodynamic size of the nanoparticles and conjugates dispersed in PBS were characterized by dynamic light scattering, and the results are shown in Figure 3b. A reasonable increment in the hydrodynamic size of the conjugates indicates the successful construction of the $NaGdF_4$:Yb,Er@$NaGdF_4$-MGb_2 (NP-MGb_2) probe. The number of MGb_2 molecules per NP was determined to be ~3.8 according to the method previously reported.[13] The resulting conjugates turned out to be very stable by showing nearly no change in both size and size distribution, after being stored at 4 °C in PBS over 1 year (Figure S2). By using the same approach, the $NaGdF_4$:Yb,Er@$NaGdF_4$-mIgG (NP-mIgG) conjugate was also constructed and used as a negative control for *in vitro* cell staining.

The MGb_2 antigen has been demonstrated to be highly expressed on the gastric cancer cell line SGC7901.[33] Thus, SGC7901 cells were used for evaluating the specific binding affinity of the NP-MGb_2 probe through cell-staining experiments. After incubation with the probes at 37 °C for 1 h, the cells were washed with PBS and subjected to confocal imaging using a 980 nm laser. The typical upconversion luminescence images were captured and then merged with the images of nuclei stained by Hoechst. As displayed in

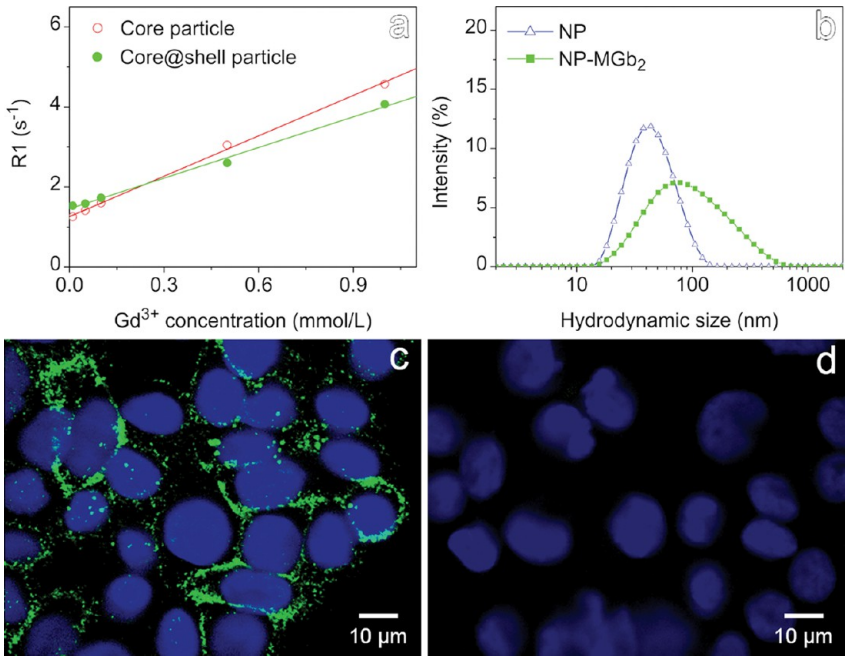

Figure 3. (a) T_1 relaxation rate (R_1) of PEGylated core particles and core@shell particles in water against the concentration of Gd^{3+} determined on 3T clinical MRI instrument. (b) Size distribution profiles of the PEGylated particles and the particle-antibody conjugates (NP-MGb$_2$) determined by dynamic light scattering. (c,d) Upconversion luminescence images overlapped with fluorescence images of nuclei stained by Hoechst for SGC7901 cells obtained after incubation with NP-MGb$_2$ (c) and NP-mIgG (d).

Figure 3c, the upconversion signals (green) from the NP-MGb$_2$ probes are predominantly located at the cell membrane. In contrast, no upconversion signal is presented by the SGC7901 cells incubated with the NP-mIgG probe, as shown in Figure 3d. This indicates that the NP-MGb$_2$ probes possess outstanding specific binding specificity for the target cells.

Establishment and Verification of the Orthotopic Tumor Model. In order to demonstrate the *in vivo* imaging capability of the NP-MGb$_2$ probe, an orthotopic gastric tumor model was established by a surgical procedure.[34] To monitor the tumor growth, a stably luciferase-expressing SGC7901 cell line (SGC7901-Luc) was used to enable constant monitoring of tumor development. Ten days after surgical implantation of the tumor cells into the stomach subserosa layer, the nude mice were screened by bioluminescence imaging (BLI) to verify successful inoculation. Two representative BLI pictures of mice bearing orthotopically implanted tumors are shown in Figure S3. Only mice exhibiting comparable bioluminescence intensities were chosen for parallel studies.

***In Vivo* MR Imaging of Orthotopically Implanted Tumors.** To verify the tumor-targeting ability, tumor-bearing mice were subjected to MRI measurements after intravenous delivery of the NP-MGb$_2$ probe through tail vein injection. As shown in Figure S4, the significantly decreased relative T_1 value at 4 h postinjection with reference to the control experiments demonstrates the specific targeting ability of the NP-MGb$_2$ probe to the orthotopically implanted tumor *in vivo*. It should be mentioned that the MRI experiments were carried out in a preliminary study 20 days after the inoculation of tumor cells to confirm that the tumor did grow on the stomach. The upconversion luminescence imaging was subsequently carried out on mice 10 days after the inoculation of tumor cells to reveal the imaging ability of the core@shell particle-based probe for small tumors.

***In Vivo* Upconversion Luminescence Imaging of GC Tumors.** The upconversion luminescence images were acquired at specific time points of 4, 6, and 8 h, which were carefully chosen based on the aforementioned MRI results. The luminescence images merged with bright-field images for an individual animal are shown in Figure 4a. Two clearly identifiable luminescence signals in the stomach region can be observed at each time point after injection of the NP-MGb$_2$ probe. The edges of the signal regions are clearly delineated from surrounding tissue in the luminescence images. This is a noteworthy observation, indicating complete absence of the autofluorescence from the surrounding tissue under the 980 nm excitation and distinguishing the UCNPs used here from many other fluorescent probes. The quantitative signal intensities at different time points were further analyzed by the Andor Solis software and are provided in Figure S5. The peak intensity of the relatively larger region, as indicated by the red arrow in Figure 4b, was achieved at 4 h postinjection, while that of the relatively smaller region was achieved at 6 h postinjection. The SNR at the region of interest shown in Figure 4b was calculated

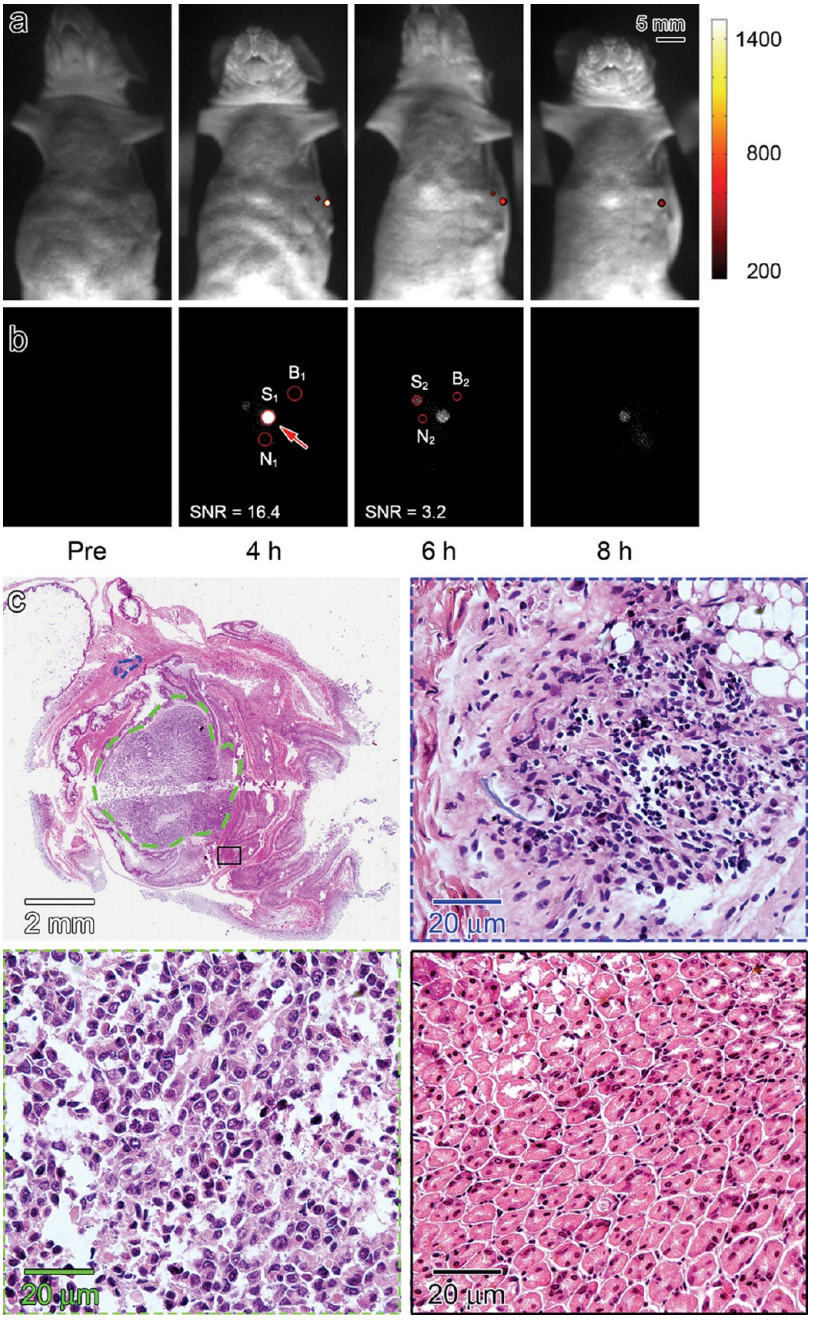

Figure 4. *In vivo* **optical images obtained before and at different time points after intravenous injection of the NP-MGb$_2$ probe: bright-field images superimposed with color-coded upconversion luminescence images (a). Luminescence signals of different sites labeled S for signal, N for noise, and B for background to determine SNR (b). Histopathological images of the stomach showing two malignant lesions highlighted by green and blue dashed lines to compare with normal stomach tissue in a solid black square, together with the enlarged images for these areas (c).**

by [*S* (signal intensity) − *B* (background signal intensity)]/[*N* (noise signal intensity) − *B* (background signal intensity)]. The SNR of the larger region at 4 h was 16.4, and the smaller one at 6 h was 3.2.

To investigate the two luminescent signals that present different time evolutions, the mouse was sacrificed right after the imaging experiments; the stomach was extracted and subjected to histopathological analysis with hematoxylin and eosin (H&E) staining. Two distinguished tumor lesions were observed from the stomach, as shown in Figure 4c. According to the microscopic image, the sizes of the lesions were determined to be approximately 4.4 and 0.80 mm. The larger lesion indicated by the green circle and the smaller lesion by the blue circle present a moderately differentiated and highly mitotic phenotype, distinct from the normal stomach tissue morphous enlarged from the black square. Most importantly, the relative position of these two tumor lesions is consistent with the imaging results, which

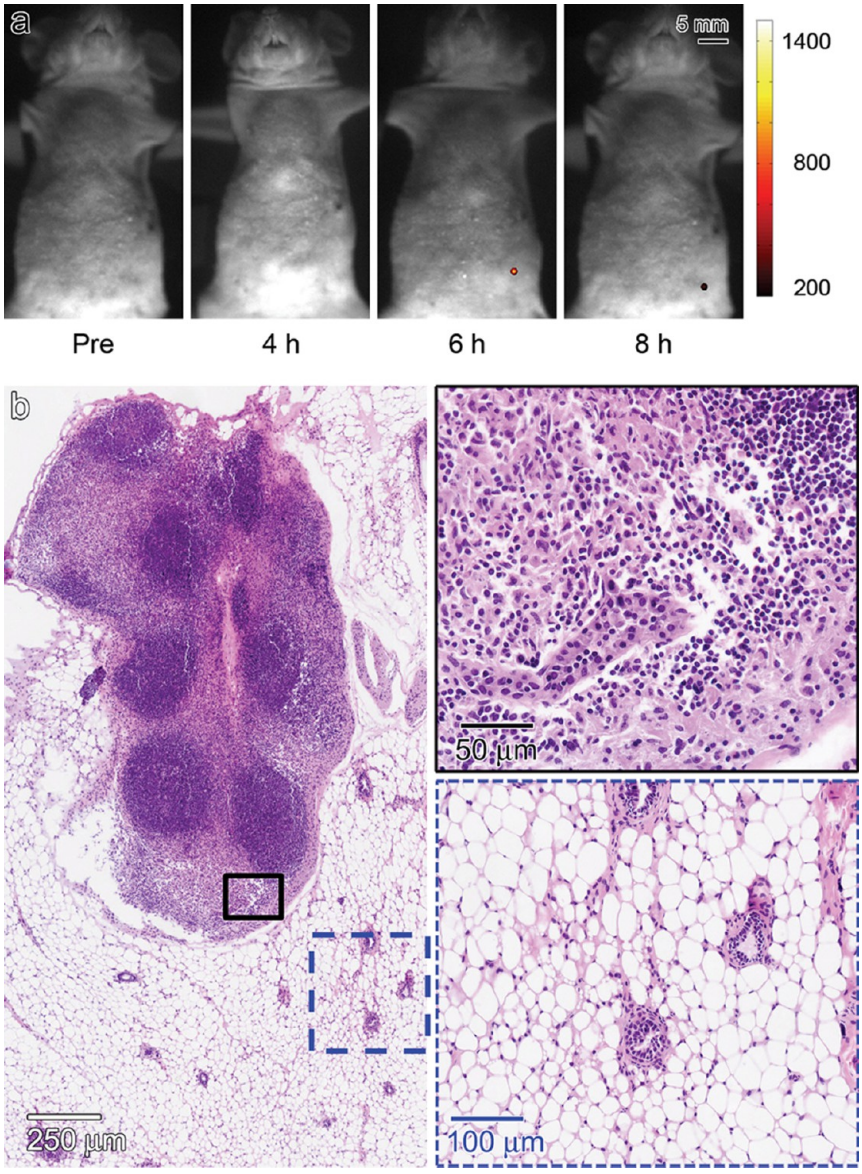

Figure 5. (a) *In vivo* optical images obtained before and at different time points after intravenous injection of the NP-MGb_2 probe into a purposely chosen mouse showing relatively low BLI signal. (b) Histopathological image of the identified LN exhibiting upconversion luminescence. Part of the malignant node and the surrounding vasculature are enlarged to better show the metastatic characteristics.

strongly confirms that the two luminescent signals come from these tumor lesions in the stomach. Furthermore, systematic study of the whole section series acquired from the stomach revealed that the smaller lesion was a lymphatic vessel adjacent to the cardia of the stomach. However, these two lesions were not differentiated by BLI, quite probably because the luciferase-induced bioluminescence signal will spread within the tumor region due to the diffusion of luciferyl adenylate.

To further challenge the ability of the NP-MGb_2 probe to image smaller tumors, a mouse that exhibited lower BLI intensity from the implanted tumor (Figure S3B) was purposely chosen for the following upconversion luminescence imaging experiments. A signal from the abdominal region, as shown in Figure 5a, was detected 6 h after the intravenous injection of the NP-MGb_2 probe, consistent with the observation for lymphatic metastasis shown in Figure 4 but longer than that required for the primary tumor (4 h postinjection). After 8 h, the mouse was sacrificed and the tissue with the signal was obtained by operation under the guidance of the luminescence. It is worth mentioning that the tissue with an optical signal was clearly distinguished from the surrounding, non-emitting tissue, and the luminescence was essential for guiding excision. Histopathological analyses shown in Figure 5b confirm that the signal is in fact from an omental lymph node, a typical metastatic site for GC, rather than the inoculation site. The enlarged views

taken from Figure 5b show part of the lymph node (black square) and surrounding vasculature (blue square) where tumor cells can be identified. This stimulating observation strongly supports the imaging results on lymphatic metastasis in the perigastric region shown in Figure 4 and further highlights the ability of the NP-MGb_2 probe for LN metastasis imaging. Intraperitoneal injection of luciferin for BLI failed to indicate the current metastatic LN (Figure S3B), probably caused by sophisticated barriers blocking the access of luciferin due to the different delivery method compared to tail vein injection of the NP-MGb_2 probe.

As a matter of fact, the intravenous delivery of nanoprobes strongly relies on the vascular architecture of the tumor.[35] To explain the absence of a luminescent signal from the originally transplanted tumor, the stomach was extracted for immunohistochemical analysis. According to staining results for CD34, as shown in Figure S6A, a lack of vasculature in the center area of the tumor (red circle) compared to the normal gastric tissue was immediately evident, which is also consistent with previous studies that show that some tumors may remain avascular until the expansion of the tumor beyond a diameter of 1−2 mm.[36] Rather consistently, the tumor on the stomach is around 0.7 mm in diameter according to the H&E stained slide shown in Figure S6B. Thus, delivery of the nanoprobes to the tumor lesion was limited by the lack of vascular in the small tumor. However, the lesion in the metastatic site was still detected by the injected probes, which have presumably accessed the lymphatic vessels by conventional drainage *via* the interstitium.[37−39]

DISCUSSION

Lymphatic status is a very important factor for the prognosis of cancer patients. With respect to the detection of LN metastasis, no imaging modality consistently achieves both high sensitivity and high specificity. Among different imaging modalities, such as abdominal ultrasonography, endoscopic ultrasonography, multidetector-row computed tomography, MRI, and ^{18}F-fluoro-2-deoxyglucose positron emission tomography (FDG-PET), FDG-PET presents high specificity, although the sensitivity varies from poor to moderate.[3] This is because the spatial resolution of FDG-PET (*i.e.*, 4−5 mm) is larger than the size of a significant proportion of metastatic LNs in gastric cancer, which are typically smaller than 3 mm.[40] Low uptake of FDG by metastatic LNs also adds to the poor-to-moderate sensitivity of FDG-PET. In addition, the FDG uptake by the adjacent primary tumor and stomach tissue also gives rise to high background noise and masks the detection of perigastric LNs.[3]

In contrast, the sensitivity and specificity achieved by using the current UCNP-based probes are apparently superior to FDG-PET and other techniques for differentiating lymphatic metastasis from the primary tumor due to the following reasons. First, the PEG coating provides excellent blood circulation behavior and ensures that the nanoparticle circulates and penetrates into the tumor interstitium followed by drainage to the lymphatic system, which is favorable for tumor and lymphatic metastasis imaging. Second, the favorable uptake and retention of the nanoprobes by the tumor and LNs contribute to the imaging specificity. Third, the surface-binding tumor-specific antibody greatly increases the binding affinity of the current probe to the tumor and lymphatic metastasis, which is conclusively supported by the control imaging experiments based on irrelevant conjugate NP-mIgG, nonfunctionalized particles, and a blocking experiment upon preadministration of MGb_2 followed by NP-MGb_2, as shown in Figure S7. Fourth, the remarkably enhanced luminescence achieved by core@shell structuring ensures high sensitivity for detection. Last but not least, extremely low background of upconversion emission from the surrounding stroma and food residue in the stomach contributes further to the sensitivity.

In fact, MR imaging of lymph nodes enhanced by ultrasmall superparamagnetic iron oxide nanoparticles was reported quite some time ago. The mechanism largely relies on populating differences of macrophages between benign and malignant nodes,[38] which makes detection of micrometatasis in LNs difficult. However, the current study provides a different mechanism for imaging only lymph nodes positive for metastases through active targeting of the malignant nodes *via* specific antibody−antigen recognition. Although the targeting ability of nanoparticle−mAb conjugates may suffer from the adsorption of additional proteins under physiological conditions,[41,42] the successful *in vivo* imaging of the orthotopic tumor and lymphatic metastasis indicated that if the nonspecific adsorption of plasma proteins would occur with respect to the current NP-MGb_2 probe, it might be at a very low level and may even be negligible. Since no benign lymph node exhibited detectable luminescence during the whole time window, it can be concluded that the antibiofouling modification effectively prevents the nanoprobe from being taken up by LNs, which is usually mediated by nonspecific adsorption of proteins on the particulate probe surface. Both of the smaller lesions in the first case at secondary sites (Figure 4) and the lymph node lesion in the second case (Figure 5) were all detected while having a size smaller than 1 mm. Results from both of these cases strongly indicate that optical imaging with the UCNP probes can potentially be developed for detecting micrometastasis of gastric cancer.

Although optical imaging offers an ultrasensitive tool for tumor detection, the limited tissue penetration is widely accepted to be a flaw of optical imaging. However, gastric cancer, as well as other digestive

diseases, can be easily examined by endoscopy. Therefore, the optical signal does not always need to penetrate through the whole abdominal wall to be detected. The endoscopes capable of detecting fluorescent signals are largely developed so far and are waiting for suitable tumor-specific diagnostic probes, which merits the current investigations.

CONCLUSIONS

In summary, core@shell structured $NaGdF_4$:Yb,Er@$NaGdF_4$ nanoparticles, with greatly enhanced luminescence intensity compared to the core nanoparticles, have been synthesized for constructing a highly specific gastric tumor probe. *In vivo* upconversion luminescence imaging studies on orthotopic models combined with the histopathological/immunohistochemical assays have demonstrated the outstanding ability of the imaging probe for detecting very small lesions at primary and lymphatic metastatic sites, owing to the excellent tumor-targeting specificity and imaging sensitivity enabled by the rational probe design. Therefore, the current studies may pave a highly effective approach for GC diagnosis as well as provide a powerful tool for distinguishing benign and malignant lymph nodes or even detecting tiny lymphatic metastasis during surgical lymphadenectomy.

EXPERIMENTAL SECTION

Chemicals. The following materials were purchased from Sigma-Aldrich: $GdCl_3 \cdot 6H_2O$ (450855), $YbCl_3 \cdot 6H_2O$ (337927), $ErCl_3 \cdot 6H_2O$ (259256), oleic acid (OA, 364525), 1-octadecene (ODE, O806), ammonium fluoride (NH_4F, 216011), tris(2-carboxyethyl)phosphine hydrochloride (TCEP, C4706), and murine immunoglobulin G (mIgG, I5381). Analytical grade chemicals such as ethanol, cyclohexane, and tetrahydrofuran (THF) were purchased from Sinopharm Chemical Reagent Beijing, Co., Ltd. Mal-PEG-dp was a customized product provided by Beijing Oneder Hightech Co. Ltd. Human gastric cancer cell line SGC7901, SGC7901-Luc cells, and MGb_2 monoclonal antibody were obtained from the Fourth Military Medical University (FMMU). Rat anti-mouse CD34 antibody and secondary horseradish peroxidase (HRP)-labeled rabbit anti-rat IgG antibody were purchased from BD Biosciences.

Preparation of $NaGdF_4$:Yb,Er Core Nanocrystals. $NaGdF_4$:Yb,Er core nanocrystals (13.8 nm) were synthesized according to our previous reports.[8] Typically, $GdCl_3 \cdot 6H_2O$ (0.80 mmol), $YbCl_3 \cdot 6H_2O$ (0.18 mmol), and $ErCl_3 \cdot 6H_2O$ (0.02 mmol) were mixed with 14 mL of OA and 16 mL of ODE in a 100 mL flask. The resultant mixture was heated to 150 °C to form a homogeneous solution under reduced pressure. After the solution was cooled to 50 °C, 10 mL of methanol solution containing NaOH (2.5 mmol) and NH_4F (4 mmol) was slowly introduced, and the reaction system was then kept under stirring at 50 °C for 30 min. Subsequently, methanol in the system was removed by keeping the reaction system at 100 °C for 10 min under reduced pressure. Under atmospheric pressure, the finally formed reaction mixture was heated to 300 °C. The reactions were held for 1 h under nitrogen protection and then terminated by cooling the reaction mixture to room temperature. The resultant nanoparticles were precipitated by ethanol, collected by centrifugation, washed with ethanol for several cycles, and finally redispersed in THF or cyclohexane for further experiments.

Preparation of Core@Shell Structured $NaGdF_4$:Yb,Er@$NaGdF_4$ Nanocrystals. Typically, 6 mL of cyclohexane solution of the purified $NaGdF_4$:Yb,Er core nanocrystals was mixed with $GdCl_3 \cdot 6H_2O$ (0.50 mmol), 4 mL of OA, and 16 mL of ODE in a 100 mL flask. The growth of the $NaGdF_4$ shell and the following purification procedures for the core@shell particles were the same as those for the core nanocrystals. The purified nanoparticles were also redispersed in THF or cyclohexane for further experiments.

Ligand Exchange. Approximately 10 mg of the purified particles ($NaGdF_4$:Yb,Er or $NaGdF_4$:Yb,Er@$NaGdF_4$) and 100 mg of mal-PEG-dp were dissolved in 5 mL of THF. The ligand exchange reaction took place overnight at 40 °C. Then, the PEGylated particles were precipitated by cyclohexane, washed with cyclohexane three times, and finally dried under vacuum at room temperature. The upconversion fluorescence emissions of the PEG-coated core or core@shell nanoparticles in Milli-Q water were recorded by a fluorescence spectrometer with a constant excitation power density. Since the resulting PEGylated particles have rather comparable particle size, surface coating, and similar particle core composition in comparison with those previously reported,[12,13] low cytotoxicity is reasonably expected.

Characterization of Core and Core@Shell Nanocrystals. TEM images were obtained with a JEM-100CXII microscope operating at an accelerating voltage of 100 kV to characterize the particle size. The concentration of the rare-earth elements in different systems was determined by using an inductively coupled plasma atomic emission spectrometer produced by Jiangsu Skyray Instrument Co., Ltd. after the particles were eroded with concentrated nitric acid. The upconversion fluorescence spectra were recorded on a Cary Eclipse fluorescence spectrophotometer equipped with a 980 nm CW laser diode (2 W) serving as the excitation source.

Preparation of the $NaGdF_4$:Yb,Er@$NaGdF_4$-MGb_2 (NP-MGb_2) Probe. Typically, MGb_2 monoclonal antibody (1 mg/mL in 10×PBS) was subjected to mild reduction by TCEP to convert the disulfide groups in the Fc fragments to thiol groups. The partially reduced mAb was purified by using 30-K MWCO centrifugal devices (Millipore YM-30). The NP-MGb_2 probe was prepared by conjugating the partially reduced MGb_2 mAb with (mal-PEG-dp)-coated core@shell nanoparticles in Tris-buffered saline (pH 7.04) through "click" reation. The molar ratio of particle-to-antibody was 1:4. By labeling the antibody with fluorescein isothiocyanate, the conversion rate of the antibody was determined to be around 95%.[13] Thus, the number of MGb_2 molecules was estimated to be ~3.8 per particle.

The resultant conjugate NP-MGb_2 was transferred into 1×PBS buffer and stored at 4 °C for further use. In a similar way, a reference probe NP-mIgG was prepared. The formation of the conjugates was investigated by dynamic light scattering.

Cell Culture. A gastric cancer cell line, SGC7901, was cultured in RPMI 1640 medium (HyClone) supplemented with 10% fetal bovine serum (HyClone; Thermo Scientific), 100 U/mL penicillin, and 0.1 mg/mL streptomycin at 37 °C under 5% CO_2.

Confocal Microscopic Imaging of Cells Labeled with the NP-MGb_2 Probe. SGC7901 cells were seeded on a Nunc Lab-Tek II 8-well chamber slide system and incubated overnight at 37 °C under 5% CO_2 to allow a firm adherence. After being rinsed with PBS buffer, the cells were fixed with 4% paraformaldehyde for 10 min and washed three times with PBS and then incubated with NP-MGb_2 conjugates and NP-mIgG conjugates at 37 °C under 5% CO_2 for 2 h. Subsequently, the cells were rinsed three times with PBS buffer to remove the unbound probes. The cells were further incubated with 5 μg/mL Hoechst 33258 for nuclei staining. Fluorescence imaging was conducted on a Zeiss LSM 780 confocal microscope equipped with Spectra-Physics MaiTai Ti:sapphire laser (100 fs, 80 MHz repetition rate). For cell imaging, the wavelength of the laser source was tuned to 980 nm for exciting the particles, while luminescence signals were collected through a 32 channel GaAsP PMT detector in a wavelength range of 500−700 nm. For the nuclei imaging, the excitation line was tuned to 405 nm and the fluorescence signals were collected in a range of 420−520 nm.

Orthotopic Mouse Model of Human Gastric Cancer. Female athymic BALB/c nude mice about 6 weeks old were obtained from the Animal Experimental Center of Slaccas (Shanghai, China) for the construction of the orthotopic tumor model. The mice were anesthetized with ketamine and xylazine. A 2−3 cm left abdominal incision was carefully made to expose the stomach of the mouse. Approximately 5×10^6 SGC7901-Luc cells suspended in 50 μL of medium were orthotopically inoculated into the subserosa layer of the gastric wall by using 30 gauge needles (Becton; Dickinson and Company). The microinjection site was pressed with a cotton swab for several minutes to prevent cell suspension effusing to unwanted regions. The stomach was then returned to the peritoneal cavity, and the abdominal wall and skin were then sutured with prolene. All animal protocols were approved by the Animal Welfare and Ethics Committee of FMMU.

Bioluminescence Imaging of the Implanted Tumors. Ten days after the inoculation of the SGC7901-Luc cells, the mice were anesthetized with isofluorane and then filter-sterilized D-luciferin solution (150 mg/kg body weight) was intraperitoneally injected. After 10 min, the bioluminescence images were acquired with an IVIS Lumina II *in vivo* imaging system (Caliper Life Sciences, Inc.), and the optical signal was expressed as total radiance in units of p/s/cm^2/sr within the region of interest. A total of 16 female athymic BALB/c nude mice were utilized in this study. Four failed to be successfully inoculated, two exhibited tumors in multiple sites, and three exhibited bioluminescence lower than expected. The remaining animals were used for the current study.

***In Vivo* Magnetic Resonance Imaging of Tumors.** Twenty days after the orthotopic model was established, the nanoprobes were administered by tail vein injection after anesthetization (n = 3 per group). The MR images were acquired on a 7 T animal MRI instrument (Bruker 7T HD, Milwaukee, WI) at designed time points postinjection. For the T_1-weighted fast spin echo imaging, the detailed imaging parameters were set as follows: field of view (FOV) = 3.5 × 3.5 cm^2; matrix size = 256 × 256; slice thickness = 1 mm; echo time (TE) = 8 ms; repetition time (TR) = 300 ms; number of excitations (NEX) = 3. The T_1 values were acquired from a T_1 mapping sequence with parameters set as follows: FOV = 3.5 × 3.5 cm^2; matrix size = 256 × 256; slice thickness = 1 mm; TE = 20 ms; TR = 800, 1500, 3000, 5000 ms; NEX = 3.

***In Vivo* Upconversion Luminescence Imaging of Tumors.** The dose level was set to 15 mg of Gd per kilogram body weight for NP-MGb$_2$ and NP-mIgG probes for all *in vivo* experiments. The upconversion luminescence images of tumors were captured by using a cooled electron-multiplying charge-coupled device (iXon, 888Andor) equipped with a 400−750 nm band-pass filter set (AZURE Photonics Co., Ltd.). A 0−30 W adjustable CW 980 nm laser (Hi-Tech Optoelectronics Co., Ltd.) was used as an excitation source with a beam size of 20 mm, larger than the size of the stomach. The excitation light density was ~320 mW/cm^2. The distance between the skin on top of the tumor and the laser diode was approximately 40 mm. Images of luminescent signals were analyzed with Andor Solis Software, and the superimposed images were constructed by overlaying luminescent images on bright-field images with Matlab.

Histopathological Assay. The stomachs were harvested and then fixed in 10% formalin for 3 days. After being embedded into paraffin, contiguous sections (4 μm) were obtained and stained with H&E and then subjected to microscopic observation. The stained slices were analyzed by two independent pathologists at FMMU.

Immunohistochemical Assay. Tumor vasculature was stained for CD34. In detail, 5 μm thick sections were placed onto slides and incubated at 60 °C for 20 min. The tumor sections on the slides were deparaffinized and dehydrated by sequentially passing through 100% dimethylbenzene, 100% dimethylbenzene, 100% EtOH, 95% EtOH, and 75% EtOH, and then transferred into sodium citrate buffer (pH = 6.0) and heated to 100 °C for 3 min. After being cooled to room temperature, the slides were washed three times (5 min each time) with Tris-buffered saline with Tween (TBST) and then incubated in 0.3% H_2O_2 for 15 min and washed three times again with TBST. Blocking was performed with 10% goat serum for 2 h at room temperature. Primary rat anti-mouse CD34 antibody was immediately applied after removing the block serum, and the slides were incubated overnight at 4 °C. After incubation, sections were washed with TBST three times and incubated with secondary HRP-labeled rabbit anti-rat IgG antibody for 1 h. Chromogen was developed using the glucose oxidase-diaminobenzidine method, and CD34 staining was visualized by its characteristic brown color. Nuclei were stained with hematoxylin and visualized as a light blue color. Slides were then rinsed in running tap water for 5 min and dehydrated, cleaned, and mounted for further histopathological examination.

Conflict of Interest: The authors declare no competing financial interest.

Acknowledgment. The authors thank the National Basic Research Program of China (2011CB935800), NSFC (81090271, 21003135, 21203211, 21321063, 21203210), and CAS (CMS-PY-201309) for financial support. The authors are grateful for Dr. Rongcheng Han from IGDB of CAS for his great help with the confocal microscopy experiments. R.Q. also thanks Dr. Ivan Kempson from Ian Wark Research Institute of UniSA for stimulating discussion.

Supporting Information Available: (1) Normalized luminescence spectra of PEGylated core particle and core@shell particle in water recorded under excitation at 980 nm. (2) Hydrodynamic size distribution profiles of the NP-MGb$_2$ conjugates determined right after synthesis and 1 year storage at 4 °C. (3) Bioluminescence images of orthotopic tumor models used for *in vivo* tumor imaging. (4) MR imaging of gastric tumor in orthotopic models. (5) Temporal evolutions of integrated photoluminescence extracted from the larger tumor lesion and smaller tumor lesion in Figure 4b. (6) Representative H&E staining image and an immunohistochemical staining image of the primary tumor lesion. (7) Bright-field images superimposed with upconversion luminescence images of control groups. This material is available free of charge *via* the Internet at http://pubs.acs.org.

REFERENCES AND NOTES

1. González, C. A.; Agudo, A. Carcinogenesis, Prevention and Early Detection of Gastric Cancer: Where We Are and Where We Should Go. *Int. J. Cancer* **2012**, *130*, 745–753.
2. Li, H.; Lu, P.; Lu, Y.; Liu, C. G.; Xu, H. M.; Wang, S. B.; Chen, J. Q. Predictive Factors for Lymph Node Metastasis in Poorly Differentiated Early Gastric Cancer and Their Impact on the Surgical Strategy. *World J. Gastroenterol.* **2008**, *14*, 4222–4226.
3. Kwee, R. M.; Kwee, T. C. Imaging in Assessing Lymph Node Status in Gastric Cancer. *Gastric Cancer* **2009**, *12*, 6–22.
4. Weissleder, R. Molecular Imaging in Cancer. *Science* **2006**, *312*, 1168–1171.
5. Weissleder, R.; Pittet, M. J. Imaging in the Era of Molecular Oncology. *Nature* **2008**, *452*, 580–589.
6. Ito, A.; Ito, Y.; Matsushima, S.; Tsuchida, D.; Ogasawara, M.; Hasegawa, J.; Misawa, K.; Kondo, E.; Kaneda, N.; Nakanishi, H. New Whole-Body Multimodality Imaging of Gastric Cancer Peritoneal Metastasis Combining Fluorescence Imaging with ICG-Labeled Antibody and MRI in Mice. *Gastric Cancer* **2014**, *17*, 497–507.
7. Zhou, J.; Liu, Z.; Li, F. Y. Upconversion Nanophosphors for Small-Animal Imaging. *Chem. Soc. Rev.* **2012**, *41*, 1323–1349.
8. Liu, C.; Hou, Y.; Gao, M. Y. Are Rare-Earth Nanoparticles Suitable for *in Vivo* Applications? *Adv. Mater.* **2014**, *26*, 6922–6932.
9. Wang, F.; Liu, X. G. Recent Advances in the Chemistry of Lanthanide-Doped Upconversion Nanocrystals. *Chem. Soc. Rev.* **2009**, *38*, 976–989.
10. Wu, S. W.; Han, G.; Milliron, D. J.; Aloni, S.; Altoe, V.; Talapin, D. V.; Cohen, B. E.; Schuck, P. J. Non-blinking and Photostable Upconverted Luminescence from Single

Lanthanide-Doped Nanocrystals. *Proc. Natl. Acad. Sci. U.S. A.* **2009**, *106*, 10917–10921.
11. Park, Y. I.; Kim, J. H.; Lee, K. T.; Jeon, K. S.; Bin Na, H.; Yu, J. H.; Kim, H. M.; Lee, N.; Choi, S. H.; Baik, S. I.; et al. Nonblinking and Nonbleaching Upconverting Nanoparticles as an Optical Imaging Nanoprobe and T_1 Magnetic Resonance Imaging Contrast Agent. *Adv. Mater.* **2009**, *21*, 4467–4471.
12. Hou, Y.; Qiao, R. R.; Fang, F.; Wang, X. X.; Dong, C. Y.; Liu, K.; Liu, C. Y.; Liu, Z. F.; Lei, H.; Wang, F.; et al. $NaGdF_4$ Nanoparticle-Based Molecular Probes for Magnetic Resonance Imaging of Intraperitoneal Tumor Xenografts *in Vivo*. *ACS Nano* **2013**, *7*, 330–338.
13. Liu, C. Y.; Gao, Z. Y.; Zeng, J. F.; Hou, Y.; Fang, F.; Li, Y. L.; Qiao, R. R.; Shen, L.; Lei, H.; Yang, W. S.; et al. Magnetic/Upconversion Fluorescent $NaGdF_4$:Yb,Er Nanoparticle-Based Dual-Modal Molecular Probes for Imaging Tiny Tumors *in Vivo*. *ACS Nano* **2013**, *7*, 7227–7240.
14. Chen, G. Y.; Ohulchanskyy, T. Y.; Liu, S.; Law, W. C.; Wu, F.; Swihart, M. T.; Agren, H.; Prasad, P. N. Core/Shell $NaGdF_4$:Nd^{3+}/$NaGdF_4$ Nanocrystals with Efficient Near-Infrared to Near-Infrared Downconversion Photoluminescence for Bioimaging Applications. *ACS Nano* **2012**, *6*, 2969–2977.
15. Xiong, L. Q.; Chen, Z. G.; Yu, M. X.; Li, F. Y.; Liu, C.; Huang, C. H. Synthesis, Characterization, and *in Vivo* Targeted Imaging of Amine-Functionalized Rare-Earth Up-converting Nanophosphors. *Biomaterials* **2009**, *30*, 5592–5600.
16. Zako, T.; Nagata, H.; Terada, N.; Utsumi, A.; Sakono, M.; Yohda, M.; Ueda, H.; Soga, K.; Maeda, M. Cyclic RGD Peptide-Labeled Upconversion Nanophosphors for Tumor Cell-Targeted Imaging. *Biochem. Biophys. Res. Commun.* **2009**, *381*, 54–58.
17. Park, Y.; Kim, H. M.; Kim, J. H.; Moon, K. C.; Yoo, B.; Lee, K. T.; Lee, N.; Choi, Y.; Park, W.; Ling, D.; et al. Theranostic Probe Based on Lanthanide-Doped Nanoparticles for Simultaneous *in Vivo* Dual-Modal Imaging and Photodynamic Therapy. *Adv. Mater.* **2012**, *24*, 5755–5761.
18. Xiong, L. Q.; Chen, Z. G.; Tian, Q. W.; Cao, T. Y.; Xu, C. J.; Li, F. Y. High Contrast Upconversion Luminescence Targeted Imaging *in Vivo* Using Peptide-Labeled Nanophosphors. *Anal. Chem.* **2009**, *81*, 8687–8694.
19. Hilderbrand, S. A.; Shao, F. W.; Salthouse, C.; Mahmood, U.; Weissleder, R. Upconverting Luminescent Nanomaterials: Application to *in Vivo* Bioimaging. *Chem. Commun.* **2009**, 4188–4190.
20. Kobayashi, H.; Kosaka, N.; Ogawa, M.; Morgan, N. Y.; Smith, P. D.; Murray, C. B.; Ye, X. C.; Collins, J.; Kumar, G. A.; Bell, H.; et al. *In Vivo* Multiple Color Lymphatic Imaging Using Upconverting Nanocrystals. *J. Mater. Chem.* **2009**, *19*, 6481–6484.
21. Xiong, L. Q.; Yang, T. S.; Yang, Y.; Xu, C. J.; Li, F. Y. Long-Term *in Vivo* Biodistribution Imaging and Toxicity of Polyacrylic Acid-Coated Upconversion Nanophosphors. *Biomaterials* **2010**, *31*, 7078–7085.
22. Loi, M.; Di Paolo, D.; Becherini, P.; Zorzoli, A.; Perri, P.; Carosio, R.; Cilli, M.; Ribatti, D.; Brignole, C.; Pagnan, G.; et al. The Use of the Orthotopic Model To Validate Antivascular Therapies for Cancer. *Int. J. Dev. Biol.* **2011**, *55*, 547–555.
23. Hoffman, R. M. Orthotopic Is Orthodox: Why Are Orthotopic-Transplant Metastatic Models Different from All Other Models. *J. Cell. Biochem.* **1994**, *56*, 1–3.
24. Liu, L.; Yin, J.; Liu, C.; Guan, G.; Shi, D.; Wang, X.; Xu, B.; Tian, Z.; Zhao, J.; Nie, Y.; et al. *In Vivo* Molecular Imaging of Gastric Cancer in Human-Murine Xenograft Models with Confocal Laser Endomicroscopy Using a Tumor Vascular Homing Peptide. *Cancer Lett.* **2015**, *356*, 891–898.
25. Abel, K. A.; Boyer, J. C.; van Veggel, F. C. J. M. Hard Proof of the $NaYF_4$/$NaGdF_4$ Nanocrystal Core/Shell Structure. *J. Am. Chem. Soc.* **2009**, *131*, 14644–14645.
26. Qian, H. S.; Zhang, Y. Synthesis of Hexagonal-Phase Core–Shell $NaYF_4$ Nanocrystals with Tunable Upconversion Fluorescence. *Langmuir* **2008**, *24*, 12123–12125.
27. Li, Z. Q.; Zhang, Y.; Jiang, S. Multicolor Core/Shell-Structured Upconversion Fluorescent Nanoparticles. *Adv. Mater.* **2008**, *20*, 4765–4769.
28. Mai, H. X.; Zhang, Y. W.; Sun, L. D.; Yan, C. H. Highly Efficient Multicolor Up-conversion Emissions and Their Mechanisms of Monodisperse $NaYF_4$: Yb,Er Core and Core/Shell-Structured Nanocrystals. *J. Phys. Chem. C* **2007**, *111*, 13721–13729.
29. Vetrone, F.; Naccache, R.; Mahalingam, V.; Morgan, C. G.; Capobianco, J. A. The Active-Core/Active-Shell Approach: A Strategy To Enhance the Upconversion Luminescence in Lanthanide-Doped Nanoparticles. *Adv. Funct. Mater.* **2009**, *19*, 2924–2929.
30. Boyer, J. C.; Manseau, M. P.; Murray, J. I.; van Veggel, F. C. J. M. Surface Modification of Upconverting $NaYF_4$ Nanoparticles with PEG-Phosphate Ligands for NIR (800 nm) Biolabeling within the Biological Window. *Langmuir* **2010**, *26*, 1157–1164.
31. Johnson, N. J. J.; Oakden, W.; Stanisz, G. J.; Prosser, R. S.; van Veggel, F. C. J. M. Size-Tunable, Ultrasmall $NaGdF_4$ Nanoparticles: Insights into Their T_1 MRI Contrast Enhancement. *Chem. Mater.* **2011**, *23*, 3714–3722.
32. Fan, D. M.; Zhang, X. Y.; Chen, X. T.; Mu, Z. X.; Hu, J. L.; Qiao, T. D.; Chen, B. J. Mouse and Human Monoclonal Antibodies against Gastric Cancer. Preparation and Clinical Application. *Chin. Med. J.* **1988**, *101*, 488–489.
33. Zhang, F. M.; Ren, G.; Lu, Y. Y.; Jin, B.; Wang, J.; Chen, X.; Liu, Z. X.; Li, K.; Nie, Y. Z.; Wang, X.; et al. Identification of TRAK1 (Trafficking Protein, Kinesin-Binding 1) as MGb_2-Ag: A Novel Cancer Biomarker. *Cancer Lett.* **2009**, *274*, 250–258.
34. Hu, H.; Liu, J. T.; Yao, L. P.; Yin, J. P.; Su, N.; Liu, X. Q.; Cao, F.; Liang, J. M.; Nie, Y. Z.; Wu, K. C. Real-Time Bioluminescence and Tomographic Imaging of Gastric Cancer in a Novel Orthotopic Mouse Model. *Oncol. Rep.* **2012**, *27*, 1937–1943.
35. Prabhakar, U.; Maeda, H.; Jain, R. K.; Sevick-Muraca, E. M.; Zamboni, W.; Farokhzad, O. C.; Barry, S. T.; Gabizon, A.; Grodzinski, P.; Blakey, D. C. Challenges and Key Considerations of the Enhanced Permeability and Retention Effect for Nanomedicine Drug Delivery in Oncology. *Cancer Res.* **2013**, *73*, 2412–2417.
36. Zetter, B. R. Angiogenesis and Tumor Metastasis. *Annu. Rev. Med.* **1998**, *49*, 407–424.
37. Harisinghani, M. G.; Barentsz, J.; Hahn, P. F.; Deserno, W. M.; Tabatabaei, S.; van de Kaa, C. H.; de la Rosette, J.; Weissleder, R. Noninvasive Detection of Clinically Occult Lymph-Node Metastases in Prostate Cancer. *N. Engl. J. Med.* **2003**, *348*, 2491–2499.
38. Weissleder, R.; Elizondo, G.; Wittenberg, J.; Lee, A. S.; Josephson, L.; Brady, T. J. Ultrasmall Superparamagnetic Iron-Oxide: An Intravenous Contrast Agent for Assessing Lymph-Nodes with MR Imaging. *Radiology* **1990**, *175*, 494–498.
39. Weissleder, R.; Elizondo, G.; Wittenberg, J.; Rabito, C. A.; Bengele, H. H.; Josephson, L. Ultrasmall Superparamagnetic Iron-Oxide: Characterization of a New Class of Contrast Agents for MR Imaging. *Radiology* **1990**, *175*, 489–493.
40. Monig, S. P.; Zirbes, T. K.; Schroder, W.; Baldus, S. E.; Lindemann, D. G.; Dienes, H. P.; Holscher, A. H. Staging of Gastric Cancer: Correlation of Lymph Node Size and Metastatic Infiltration. *Am. J. Roentgenol.* **1999**, *173*, 365–367.
41. Monopoli, M. P.; Aberg, C.; Salvati, A.; Dawson, K. A. Biomolecular Coronas Provide the Biological Identity of Nanosized Materials. *Nat. Nanotechnol.* **2012**, *7*, 779–786.
42. Salvati, A.; Pitek, A. S.; Monopoli, M. P.; Prapainop, K.; Bombelli, F. B.; Hristov, D. R.; Kelly, P. M.; Aberg, C.; Mahon, E.; Dawson, K. A. Transferrin-Functionalized Nanoparticles Lose Their Targeting Capabilities When a Biomolecule Corona Adsorbs on the Surface. *Nat. Nanotechnol.* **2013**, *8*, 137–143.